

MAT: Multi-Range Attention Transformer for Efficient Image Super-Resolution

Chengxing Xie¹, Xiaoming Zhang¹, Kai Zhang², Linze Li¹, Yuqian Fu^{3,4}, Biao Gong⁵, Tianrui Li¹

¹Southwest Jiaotong University, ²Nanjing University, ³ETH Zurich, ⁴INSAIT, ⁵Ant Group

Abstract

Recent advances in image super-resolution (SR) have significantly benefited from the incorporation of Transformer architectures. However, conventional techniques aimed at enlarging the self-attention window to capture broader contexts come with inherent drawbacks, especially the significantly increased computational demands. Moreover, the feature perception within a fixed-size window of existing models restricts the effective receptive fields and the intermediate feature diversity. This study demonstrates that a flexible integration of attention across diverse spatial extents can yield significant performance enhancements. In line with this insight, we introduce **Multi-Range Attention Transformer (MAT)** tailored for SR tasks. MAT leverages the computational advantages inherent in dilation operation, in conjunction with self-attention mechanism, to facilitate both multi-range attention (MA) and sparse multi-range attention (SMA), enabling efficient capture of both regional and sparse global features. Further coupled with local feature extraction, MAT adeptly capture dependencies across various spatial ranges, improving the diversity and efficacy of its feature representations. We also introduce the MSCovStar module, which augments the model’s ability for multi-range representation learning. Comprehensive experiments show that our MAT exhibits superior performance to existing state-of-the-art SR models with remarkable efficiency ($\sim 3.3\times$ faster than SRFormer-light). Code will be released.

Introduction

Single image super-resolution (SR) is a fundamental problem in low-level computer vision, with the goal of restoring a high-resolution (HR) image from its low-resolution (LR) counterpart. The introduction of convolutional neural networks (CNNs) to SR tasks, pioneered by SRCNN (Dong et al. 2015), has led to the development of numerous CNN-based methods (Kim, Lee, and Lee 2016; Lim et al. 2017; Zhang et al. 2018a,b). However, most CNN-based models are constrained by their fixed-size convolutional kernels and local receptive fields, which prevent them from capturing global information and incorporating wider contextual knowledge into the reconstruction process.

Transformer (Vaswani et al. 2017) leverage self-attention mechanisms, enabling them to capture long-range dependencies and extract features from extensive regions. These

C. Xie and X. Zhang contribute equally to this work.

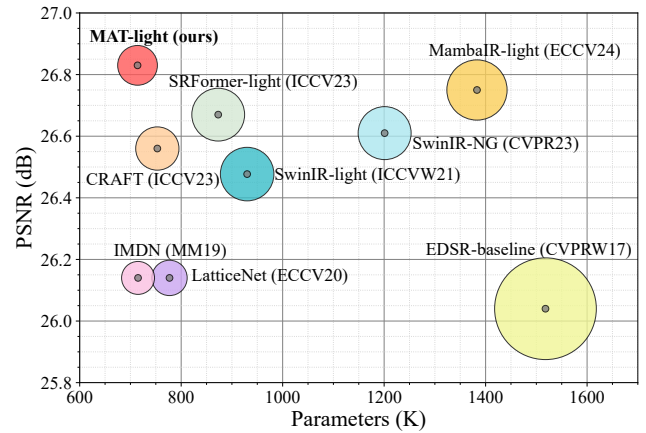


Figure 1: Comparison of trade-offs between model performance and overheads on Urban100 (Huang, Singh, and Ahuja 2015) for $\times 4$ SR. The area of each circle denotes the Multi-Adds of these models. Our MAT-Light achieves optimal SR performance with fewer parameters and Multi-Adds.

attributes are particularly advantageous for SR tasks (Gu and Dong 2021). Recent studies (Liang et al. 2021; Chen et al. 2023; Zhou et al. 2023) have demonstrated the advantages of Transformer-based models over CNN-based approaches in SR tasks, emphasizing the performance gains achieved by enlarging the windows for window self-attention (WSA) in Vision Transformers. However, directly scaling up the window size to enlarge the effective receptive field of the model can introduce a quadratic increase in computational complexity, posing challenges in terms of efficiency (Zhou et al. 2023). In addition, most existing WSA-based models rely on a singular, immovable window size (e.g., 8×8 or 16×16) to represent features, which hinders their ability to capture both local and non-local dependencies across varying spatial distances. Consequently, the main objective of this study is to achieve efficient and flexible modeling features across multiple spatial granularity.

Motivated by the commonly used dilated convolutions as explored in previous research (Chen et al. 2017b; Wang et al. 2018a), we aim to enhance the perceptual scope of attention by incorporating dilation operation without introducing additional computational burden, thus achieving an ex-

tended and efficient attention mechanism. We first substitute the convolution computation in standard convolution with attention mechanism to achieve regional attention. Then, by further adding holes into the attention region, akin to dilated convolutions, we can achieve long-range and efficient sparse global attention. To address the limitations of homogeneous operators in capturing features across different spatial ranges, we expand regional attention and sparse global attention into multi-range attention (MA) and sparse multi-range attention (SMA). MA and SMA employ multiple regional ranges to perceive features, enabling a larger effective receptive field compared to fixed-size ranges for long-range attention modeling. Unlike existing models, e.g., SwinIR (Liang et al. 2021) and ART (Zhang et al. 2023), MA and SMA introduce local inductive biases while maintaining translational equivariance, whereas the latter rely on window partitioning and lack inductive bias.

Multi-range representation learning plays a critical role in dense prediction tasks such as detection and segmentation (Redmon and Farhadi 2018; Chen et al. 2017a). In this work, we extend the concept of multi-range representation learning to SR tasks. Specifically, we attempt to exploit the hierarchical features at the local, regional, and global levels in natural images to improve the feature representations. To achieve this, we introduce the Local Aggregation Block (LAB), which leverages channel attention and convolutions to effectively aggregate local features. Then, we apply MA and SMA for extracting regional and sparse global features, respectively. Furthermore, we propose a new module named MSConvStar to replace the traditional feed-forward network (FFN). MSConvStar further enhances image token interactions by integrating multi-scale convolution (MSConv) with star operation (Ma et al. 2024).

Based on the above designs, we propose a novel model for image SR, named the Multi-Range Attention Transformer (MAT). MAT effectively captures features across various spatial ranges, significantly enhancing the model’s ability to reconstruct details. For the lightweight image SR task, our MAT-light, trained only on the DIV2K (Lim et al. 2017) dataset, achieves state-of-the-art (SOTA) performance with lower computational complexity (e.g., **26.83dB**@Urban100 $\times 4$ with only **714K** parameters), as shown in Fig. 1. For the classical image SR task, our MAT also achieves better performance with lower computational complexity. In conclusion, this work makes the following key contributions:

- (1) We introduce two effective mechanisms, dubbed MA and SMA for image SR to flexibly capture multi-range regional characteristics and sparse global attributes, enhancing the multi-range representation learning in SR.
- (2) We model the multi-range hierarchical features present in images and propose a simple yet effective MSConvStar module to replace the conventional FFN, further enhancing the model’s ability to capture multi-range features.
- (3) We propose a novel and highly efficient SR architecture named **MAT**. Extensive experiments show that our MAT outperforms existing SOTA models while maintaining lower computational complexity.

Related Works

CNN-based Image SR

CNN-based methodologies have emerged as the prevailing paradigm for SR since the advent of SRCNN (Dong et al. 2015). VDSR (Kim, Lee, and Lee 2016) employs a deeper network architecture, integrating residual learning to enhance performance metrics. EDSR (Lim et al. 2017) improves the model’s capabilities by further scaling up the residual units, which have been shown to impair SR performance. RDN (Zhang et al. 2018b) incorporates dense connection to optimize the utilization of hierarchical features. Furthermore, RCAN (Zhang et al. 2018a) integrates a channel attention mechanism, allowing for dynamic adjustment of channel-wise features based on their interdependencies. SAN (Dai et al. 2019), IGNN (Zhou et al. 2020) and NLSN (Mei, Fan, and Zhou 2021) adopt non-local attention (Wang et al. 2018b) to capture global image characteristics, significantly enhancing model performance. To address the constraints of low-power devices, some works (Hui et al. 2019; Li et al. 2022) utilize information distillation structures to build lightweight models. Despite the introduction of attention mechanisms (Zhang et al. 2018a; Mei, Fan, and Zhou 2021), large kernel convolutions (Xie et al. 2023) and partial channel shifting (Zhang, Li, and Zhao 2023), the information perception range of most CNN-based SR networks remain constrained, making it difficult to model distant dependencies (Chen et al. 2023).

Transformer-based Image SR

Vision Transformer have shown exceptional efficacy across various visual tasks (Dosovitskiy et al. 2021; Liu et al. 2021; Xie et al. 2021; Carion et al. 2020; Zamir et al. 2022). Compared to CNNs, Transformers are particularly adept at capturing long-range dependencies and extracting features from expansive regions, rendering them advantageous for SR tasks. For example, SwinIR (Liang et al. 2021) effectively integrates the Swin-Transformer (Liu et al. 2021) into the base module, resulting in marked enhancements in various image restoration applications. Omni-SR (Wang et al. 2023) amplifies the model’s capabilities by concurrently modeling pixel interactions across both spatial and channel dimensions. ART (Zhang et al. 2023) extends the model’s receptive field through the application of sparse attention, but the performance improvement is relatively limited. HAT (Chen et al. 2023) and SRFormer (Zhou et al. 2023), improve SR performance by expanding the window size of self-attention mechanisms to capture a wider array of information. Nevertheless, existing SR methods employing WSA encounter challenges regarding computational efficiency when scaling the window size, as this leads to a quadratic escalation in computational complexity and consumes more memory. Furthermore, WSA relies on fixed-size window partitioning, which limits its capacity to flexibly assimilate information from varying spatial scales. This study seeks to integrate the computational characteristics of dilation operation into the self-attention mechanism, enabling a flexible expansion of the model’s effective perception range without adding extra computational overhead.

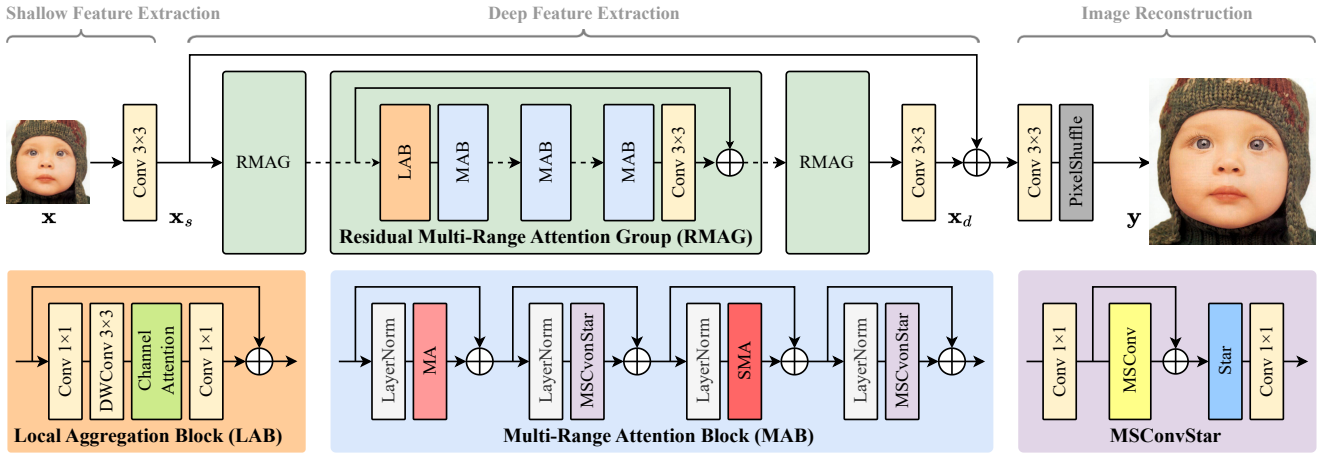


Figure 2: The overall architecture of Multi-Range Attention Transformer (MAT).

Methodology

Overall Architecture of MAT

In accordance with preceding works (Liang et al. 2021; Chen et al. 2023), the comprehensive framework of MAT is illustrated in Fig. 2, consisting of three distinct components: shallow feature extraction, deep feature extraction, and image reconstruction. Given an LR input $\mathbf{x} \in \mathbb{R}^{H \times W \times 3}$, we first use a 3×3 convolution to obtain the shallow features $\mathbf{x}_s \in \mathbb{R}^{H \times W \times C}$, where H and W denote the height and width of the input image, and C indicates the filter number of the convolution. Subsequently, \mathbf{x}_s is fed into the subnet of nonlinear inference to extract deep features $\mathbf{x}_d \in \mathbb{R}^{H \times W \times C}$ through a series of residual multi-range attention groups (RMAG) followed by a 3×3 convolution. So we can further obtain $\mathbf{x}_d \in \mathbb{R}^{H \times W \times C}$, and each RMAG is composed of an LAB, several multi-range attention blocks (MAB), a 3×3 convolution, and a residual shortcut, as shown in Fig. 2. Then, the shallow feature \mathbf{x}_s and the deep feature \mathbf{x}_d are integrated to enhance the model convergence. Finally, the reconstruction module, consisting of convolution and PixelShuffle (Shi et al. 2016), is used to reconstruct the HR image $\mathbf{y} \in \mathbb{R}^{H_{out} \times W_{out} \times 3}$, where H_{out} and W_{out} denotes the height and width of the output image respectively. The model is optimized using \mathcal{L}_1 loss between the reconstructed SR image \mathbf{y} and the ground-truth HR image.

Attention Mechanisms

Self-Attention. Self-attention (SA) (Vaswani et al. 2017) is a mechanism that transforms a query and a set of key-value pairs into an output through dot product and scaling. Given a query \mathbf{Q} , a pair of key \mathbf{K} and value \mathbf{V} , the dot product between the query and key is first computed, and scaled with a constant. The result is normalized using the softmax function to obtain the weight for the value. Afterwards, the value is multiplied by this weight to produce the outcome. The calculation can be formulated as:

$$\text{SA}(\mathbf{Q}, \mathbf{K}, \mathbf{V}) = \text{Softmax} \left(\frac{\mathbf{Q}\mathbf{K}^T}{\sqrt{d}} + B \right) \mathbf{V}, \quad (1)$$

where d is the embedding dimension and B is a learnable relative positional bias. Although SA captures well global features and enhance texture details, directly applying SA to SR tasks yield excessive noise and lead to the assignment of outsize weights, resulting in increased computational overhead (Mei, Fan, and Zhou 2021; Xia et al. 2022).

Multi-Range Attention. To strike a balance between computational complexity and performance, WSA has been widely adopted (Dosovitskiy et al. 2021; Liu et al. 2021), as illustrated in Fig. 3. However, WSA is constrained by window partitioning and inherent computational demands, restricting the flexibility in adjusting window dimensions and limit the capacity to perceive image features across a broader spatial extent. A straightforward approach is to restrict attention computation to a specified neighborhood, analogous to convolutions. Then, an effective regional attention (RA) mechanism is implemented by a calculation akin to the sliding window, characterized by a convolution-like inductive bias. Specifically, for RA with a range size of k , the key-value set corresponding to the (i, j) -th pixel $p_{i,j}$ is restricted to a $k \times k$ region, denoted as $\rho_{i,j}^k$. The RA of this pixel can be then represented as:

$$\text{RA}_k(p_{i,j}) = \text{Softmax} \left(\frac{\mathbf{Q}_{i,j} \mathbf{K}_{\rho_{i,j}^k}^T}{\sqrt{d}} + B \right) \mathbf{V}_{\rho_{i,j}^k}. \quad (2)$$

The complete RA for a given feature is achieved by iterating the above computation across all pixels within that feature. Various approaches exist to establish the concept of RA, including SASA (Ramachandran et al. 2019), NA (Hassani et al. 2023), and HaloNet (Vaswani et al. 2021). To streamline, we adopt the natten (Hassani et al. 2023) for the implementation of RA. As mentioned in the introduction, to overcome the limitations of homogeneous operators in capturing features of diverse spatial scales, we further expand RA to multi-range attention (MA):

$$\text{MA}(p_{i,j}) = H_F(\text{Concat}(\text{RA}_{k_1}, \dots, \text{RA}_{k_n})), \quad (3)$$

where k_1, \dots, k_n represent the ranges of n regions of different sizes, and H_F denotes the feature fusion module.

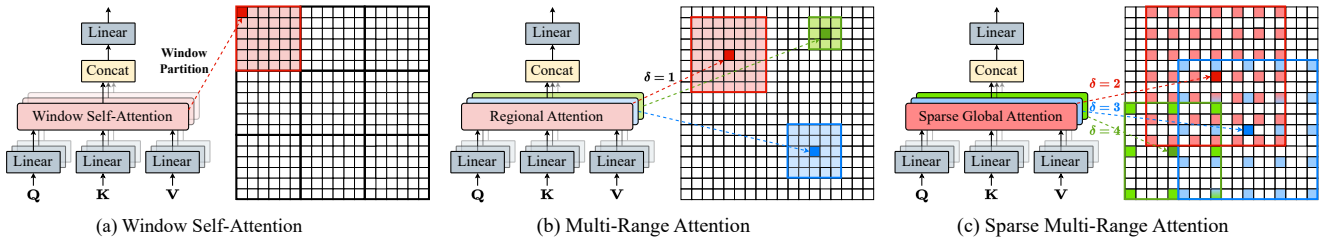


Figure 3: Illustration of the window self-attention (WSA), multi-range attention (MA) and sparse multi-range attention (SMA). MA and SMA set different range sizes and for different heads, enabling the ability of multi-range representation learning.

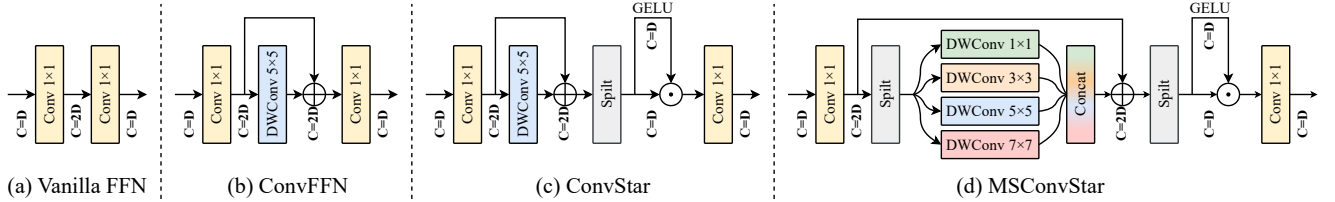


Figure 4: Illustration of FFN (Liang et al. 2021), ConvFFN (Zhou et al. 2023), ConvStar and MSConvStar. \odot : Star Operation.

By simultaneously acquiring information from different spatial ranges, MA can address the constraints associated with fixed-size window partitioning in WSA.

Sparse Multi-Range Attention. MA can be generalized to sparse multi-range attention (SMA), akin to dilated convolutions, as shown in Fig 3. Dilating the region prompts the model to capture an extended array of associations for the target pixel. We expand RA through dilation operation to achieve sparse global attention (SGA). Specifically, for SGA with a range size of k and a dilation rate of δ , the key-value set corresponding to the (i, j) -th pixel $p_{i,j}$ is limited to a sparse neighborhood of size $k_d \times k_d$, denoted as $\rho_{i,j}^{k,\delta}$, where $k_d = k + (k - 1) \cdot (\delta - 1)$. The SGA of the (i, j) -th pixel can be defined as:

$$\text{SGA}_{k,\delta}^{\delta}(p_{i,j}) = \text{Softmax} \left(\mathbf{Q}_{i,j} \mathbf{K}_{\rho_{i,j}^{k,\delta}}^T / \sqrt{d} + B \right) \mathbf{V}_{\rho_{i,j}^{k,\delta}}. \quad (4)$$

Subsequently, by aggregating SGAs from multiple ranges, we achieve SMA:

$$\text{SMA}(p_{i,j}) = H_F(\text{Concat}(\text{SGA}_{k_1}^{\delta_1}, \dots, \text{SGA}_{k_n}^{\delta_n})), \quad (5)$$

where $\delta_1, \dots, \delta_n$ represent n types of dilation rates. The sparse area size can be flexibly enlarge by adjusting dilation rates, all while without introducing computational overhead.

Multi-Range Representation Learning

MSConvStar. The vanilla feed-forward network (FFN) in the Transformer (Vaswani et al. 2017) employs two linear projection layers and an activation function, constituting a basic multilayer perceptron (MLP) designed for image token interaction. However, this MLP is inadequate for complex and hierarchical spatial relationships, thereby limiting the restoration efficacy of SR models. To address this limitation, we propose multi-scale convolution star (MSConvStar) module, which enhances image token representation by

integrating multi-scale convolution (MSConv) and star operation (Ma et al. 2024), as illustrated in Fig. 4. The parallel depth-wise convolutions of different scales and a residual connection are used to boost spatial interrelation, while the star operation facilitates the transformation of the input into a high-dimensional, non-linear feature space without necessitating an expansion of network width.

Multi-Range Dependencies. Most SR models (Lim et al. 2017; Liang et al. 2021; Li et al. 2023; Zhou et al. 2023) overlook the inherent hierarchical features present in natural images, opting for homogeneous operators for restoration modeling. In MAT, we model three types of dependencies from different spatial ranges through LAB, MA and SMA. Specifically, LAB is designed to extract relations within confined local regions, achieved through depth-wise convolutions coupled with channel attention (Zhang et al. 2018a). Then, MA and SMA are introduced to apprehend broader regional and sparse global information, respectively. Considering the weaker dependencies found in broader contexts, we integrate MA and SMA into the Transformer, and substitute the MLP layers with our MSConvStar to further enhance the multi-range representation learning.

Experiments

Experimental Settings

Datasets and Evaluation. Follow previous works (Liang et al. 2021; Zhou et al. 2023), we train two versions of MAT: lightweight and classical. For lightweight image SR, we utilize DIV2K (Lim et al. 2017) dataset to train our MAT-light. For classical version, the DF2K (DIV2K (Lim et al. 2017) + Flickr2K (Agustsson and Timofte 2017)) is employed. Our evaluation of the models is performed on five commonly used benchmark datasets, including Set5 (Bevilacqua et al. 2012), Set14 (Zeyde, Elad, and Protter 2012), B100 (Martin et al. 2001), Urban100 (Huang, Singh, and Ahuja 2015), and

Scale	Method	Annual	Params. (K)	Multi-Adds (G)	Set5 PSNR / SSIM	Set14 PSNR / SSIM	B100 PSNR / SSIM	Urban100 PSNR / SSIM	Manga109 PSNR / SSIM
×2	EDSR-baseline	CVPRW17	1370	316.3	37.99 / 0.9604	33.57 / 0.9175	32.16 / 0.8994	31.98 / 0.9272	38.54 / 0.9769
	IMDN	MM19	694	158.8	38.00 / 0.9605	33.63 / 0.9177	32.19 / 0.8996	32.17 / 0.9283	38.88 / 0.9774
	LatticeNet	ECCV20	756	169.5	38.06 / 0.9607	33.70 / 0.9187	32.20 / 0.8999	32.25 / 0.9288	-
	SwinIR-light	ICCVW21	910	252.9	38.14 / 0.9611	33.86 / 0.9206	32.31 / 0.9012	32.76 / 0.9340	39.12 / 0.9783
	SwinIR-NG	CVPR23	1181	274.1	38.17 / 0.9612	33.94 / 0.9205	32.31 / 0.9013	32.78 / 0.9340	39.20 / 0.9781
	Omni-SR	CVPR23	798	-	38.22 / 0.9613	33.98 / 0.9210	<u>32.36 / 0.9020</u>	<u>33.05 / 0.9363</u>	39.28 / 0.9784
	CRAFT	ICCV23	738	197.2	<u>38.23 / 0.9615</u>	33.92 / 0.9211	32.33 / 0.9016	32.86 / 0.9343	<u>39.39 / 0.9786</u>
	SRFormer-light	ICCV23	853	236.2	<u>38.23 / 0.9613</u>	33.94 / 0.9209	<u>32.36 / 0.9019</u>	32.91 / 0.9353	39.28 / 0.9785
	MambaIR-light	ECCV24	1363	278.9	38.16 / 0.9610	<u>34.00 / 0.9212</u>	32.34 / 0.9017	32.92 / 0.9356	39.31 / 0.9779
	MAT-light	Ours	694	189.6	38.28 / 0.9617	34.11 / 0.9227	32.41 / 0.9029	33.22 / 0.9381	39.46 / 0.9789
×3	EDSR-baseline	CVPRW17	1555	160.2	34.37 / 0.9270	30.28 / 0.8417	29.09 / 0.8052	28.15 / 0.8527	33.45 / 0.9439
	IMDN	MM19	703	71.5	34.36 / 0.9270	30.32 / 0.8417	29.09 / 0.8046	28.17 / 0.8519	33.61 / 0.9445
	LatticeNet	ECCV20	765	76.3	34.40 / 0.9272	30.32 / 0.8416	29.10 / 0.8049	28.19 / 0.8513	-
	SwinIR-light	ICCVW21	918	114.5	34.62 / 0.9289	30.54 / 0.8463	29.20 / 0.8082	28.66 / 0.8624	33.98 / 0.9478
	SwinIR-NG	CVPR23	1190	114.1	34.64 / 0.9293	30.58 / 0.8471	29.24 / 0.8090	28.75 / 0.8639	34.22 / 0.9488
	Omni-SR	CVPR23	807	-	34.70 / 0.9294	30.57 / 0.8469	29.28 / 0.8094	28.84 / 0.8656	34.22 / 0.9487
	CRAFT	ICCV23	744	87.5	34.71 / 0.9295	30.61 / 0.8469	29.24 / 0.8093	28.77 / 0.8635	34.29 / 0.9491
	SRFormer-light	ICCV23	861	104.8	34.67 / 0.9296	30.57 / 0.8469	29.26 / 0.8099	28.81 / 0.8655	34.19 / 0.9489
	MambaIR-light	ECCV24	1371	124.6	<u>34.72 / 0.9296</u>	<u>30.63 / 0.8475</u>	<u>29.29 / 0.8099</u>	<u>29.00 / 0.8689</u>	<u>34.39 / 0.9495</u>
	MAT-light	Ours	703	85.0	34.79 / 0.9303	30.68 / 0.8491	29.32 / 0.8116	29.03 / 0.8698	34.49 / 0.9505
×4	EDSR-baseline	CVPRW17	1518	114.0	32.09 / 0.8938	28.58 / 0.7813	27.57 / 0.7357	26.04 / 0.7849	30.35 / 0.9067
	IMDN	MM19	715	40.9	32.21 / 0.8948	28.58 / 0.7811	27.56 / 0.7353	26.04 / 0.7838	30.45 / 0.9075
	LatticeNet	ECCV20	777	43.6	32.18 / 0.8943	28.61 / 0.7812	27.57 / 0.7355	26.14 / 0.7844	-
	SwinIR-light	ICCVW21	930	65.2	32.44 / 0.8976	28.77 / 0.7858	27.69 / 0.7406	26.47 / 0.7980	30.92 / 0.9151
	SwinIR-NG	CVPR23	1201	63.0	32.44 / 0.8980	28.83 / 0.7870	27.73 / 0.7418	26.61 / 0.8010	31.09 / 0.9161
	Omni-SR	CVPR23	819	-	32.49 / 0.8988	28.78 / 0.7859	27.71 / 0.7415	26.64 / 0.8018	31.02 / 0.9151
	CRAFT	ICCV23	753	52.4	<u>32.52 / 0.8989</u>	28.85 / 0.7872	27.72 / 0.7418	26.56 / 0.7995	31.18 / 0.9168
	SRFormer-light	ICCV23	873	62.8	32.51 / 0.8988	28.82 / 0.7872	27.73 / 0.7422	26.67 / 0.8032	31.17 / 0.9165
	MambaIR-light	ECCV24	1383	70.8	32.51 / 0.8993	<u>28.85 / 0.7876</u>	<u>27.75 / 0.7423</u>	<u>26.75 / 0.8051</u>	<u>31.26 / 0.9175</u>
	MAT-light	Ours	714	48.5	32.61 / 0.8998	28.92 / 0.7897	27.79 / 0.7444	26.83 / 0.8088	31.38 / 0.9192

Table 1: Quantitative comparison (PSNR (dB) / SSIM) with SOTA methods for **lightweight SR** on five benchmark datasets. ‘Multi-Adds’ is calculated under the setting of upscaling one image to 1280×720 resolution. For a fair comparison, **only** the DIV2K dataset is used for training. The best and second best results are marked with bold and underline, respectively.

Manga109 (Matsui et al. 2017). The PSNR (dB) and SSIM scores, calculated on the luminance (Y) channel, are used to evaluate the performance of the model.

Implementation Details. For the lightweight image SR, we set the number of RMAG, MAB and channel to 4, 2, and 60, respectively. The range sizes of MA and SMA are both set to 7×7 , 9×9 , and 11×11 . The dilation rates of SMA are set to the floor division of the input patch size (64^2) by the range sizes. We employ the Adam optimizer (Kingma and Ba 2014) with $\beta_1 = 0.9$ and $\beta_2 = 0.99$ to train the model for a total of 500k iterations. The initial learning rate is set at 5×10^{-4} and halves at [250k, 400k, 450k, 475k]. More implementation details can refer to the *supplementary*.

Lightweight Image Super-Resolution

To demonstrate the effectiveness and efficiency of proposed model, we compare MAT-light with various recent SOTA lightweight SR methods, including the EDSR-baseline (Lim et al. 2017), IMDN (Hui et al. 2019), LatticeNet (Luo et al. 2020), SwinIR-light (Liang et al. 2021), SwinIR-NG (Choi, Lee, and Yang 2023), Omni-SR (Wang et al. 2023), CRAFT (Li et al. 2023), SRFormer-light (Zhou et al. 2023) and MambaIR-light (Guo et al. 2024).

Quantitative Comparison. Table 1 displays the quantitative comparison for lightweight image SR models. We also report the parameters and Multi-Adds of the model to provide an estimate of the efficiency and complexity. It is evident that our MAT-light demonstrates superior performance compared to other models on all five benchmark datasets across various scale factors, while also maintaining the lowest parameter count and relatively lower computational complexity. Specifically, compared to CNN-based models, our MAT-light achieves significant improvements of approximately **0.8dB** and **0.9dB** on the Urban100 and Manga109 datasets, respectively. Furthermore, when compared to Transformer-based models, our MAT-light achieves an improvement of **0.2dB~0.46dB** on the Manga109 dataset. Compared with recent Mamba-based model MambaIR-light, our MAT-light also achieves comprehensive leading results.

Visual Comparison. As shown in Fig. 5, we conduct a visual comparison between MAT-light and other lightweight image SR models. It is evident that only MAT-light successfully recovers the lines and texture details of the image. In contrast, the images recovered by other methods contain more blur artifacts and incorrect details. The visual results show the powerful reconstruction ability of MAT-light.

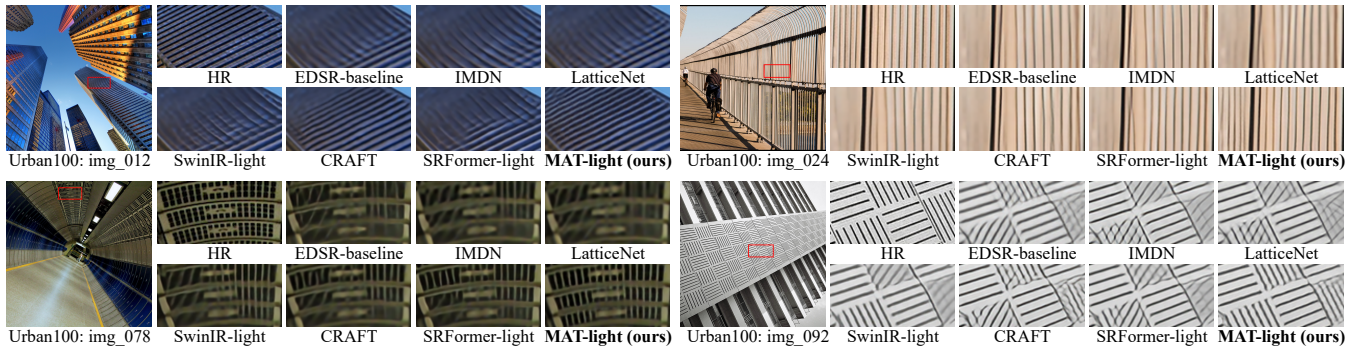


Figure 5: Visual comparison on $\times 4$ **lightweight image SR**. Comparison of classical image SR are in the *supplementary*.

Method	EDSR	RDN	RCAN	IGNN	NLSN	SwinIR	ART-S	SRFormer	MambaIR	MAT
Params. (M)	43.09	22.27	15.59	49.51	44.16	11.90	11.87	10.52	20.57	9.72
Mult-Adds (G)	205.8	93.1	65.3	-	221.8	53.8	55.6	54.3	82.2	49.2
PSNR (dB)	26.64	26.61	26.82	26.84	26.96	27.45	27.54	27.68	27.68	27.78

Table 2: Quantitative comparison ($\times 4$) with SOTA methods for **classical image SR** on Urban100 dataset. 'Multi-Adds' is calculated under the setting of upscaling one image to 256^2 resolution. More details are in the *supplementary*.

Classical Image Super-Resolution

To demonstrate MAT's scalability, we further expanded MAT to build a large model and compare it with a series of SOTA classical SR methods: EDSR (Lim et al. 2017), RCAN (Zhang et al. 2018a), IGNN (Zhou et al. 2020), NLSN (Mei, Fan, and Zhou 2021), SwinIR (Liang et al. 2021), ART (Zhang et al. 2023), SRFormer (Zhou et al. 2023) and MambaIR (Guo et al. 2024). The results presented in Table 2 highlight that MAT also achieves the best performance on classical image SR tasks with the lowest number of parameters and computational complexity. More comparison results can be found in the *supplementary*.

Ablation Study

To conduct the ablation study, we train lightweight SR models from scratch on DIV2K ($\times 2$) and evaluate the performance on Urban100 for $\times 2$ SR. All models are implemented with consistent training details to ensure a fair comparison.

Effects of Dilation Rate. By employing the dilation strategy in MAT, a wider range of information can be captured, leading to improved model performance. To explore the optimal dilation rate δ , we conducted experiments using a range of values from 1 to maximum, as presented in Table 3. Notably, $\delta = 1$ corresponds to using MA, while $\delta = \text{Maximum}$ indicates that the dilation rate for SMA is set to the floor division of the input feature map size by the range size. The results reveal that the performance improves as the dilation rate increases and achieves optimal performance when $\delta = \text{Maximum}$. In addition, we employ LAM (Gu and Dong 2021) to analyze the effect of dilation, as shown in Fig 6. It can be observed that using a larger dilation rate allows our model to perceive a larger range of information. the LAM attribution of MAT-light extends across nearly the entire image, whereas other models are confined to a limited range.

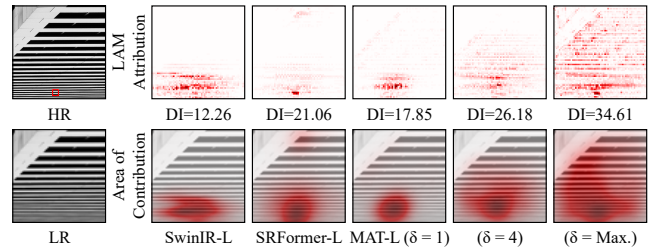


Figure 6: LAM (Gu and Dong 2021) results of SwinIR-light (Liang et al. 2021), SRFormer-light (Zhou et al. 2023) and MAT-light with various dilation rates δ . A higher diffusion index (DI) indicates a broader range of pixel activation.

δ	1	2	4	Maximum
PSNR (dB)	32.94	33.11	33.16	33.22
SSIM	0.9358	0.9373	0.9378	0.9381

Table 3: Effects of dilation rate δ . Input feature size is 64^2 .

MD	MSCConvStar	MA	Params.(K)	PSNR (dB) / SSIM
\times	\times	\times	670	32.59 / 0.9329
\checkmark	\times	\times	709	32.93 / 0.9357
\checkmark	\checkmark	\times	693	33.11 / 0.9374
\checkmark	\checkmark	\checkmark	694	33.22 / 0.9381

Table 4: Ablation study on effectiveness on each component.

Effectiveness of Each Component. We conduct a detailed ablation experiment to demonstrate the effectiveness of each proposed component, as shown in Table 4. The baseline model is derived by replacing all Transformer blocks in

Conv	Star	Multi-Scale	Params.(K)	PSNR (dB) / SSIM
✗	✗	✗	710	32.98 / 0.9359
✓	✗	✗	760	33.06 / 0.9367
✓	✓	✗	702	33.19 / 0.9379
✓	✓	✓	694	33.22 / 0.9381

Table 5: Ablation study on MSCConvStar module.

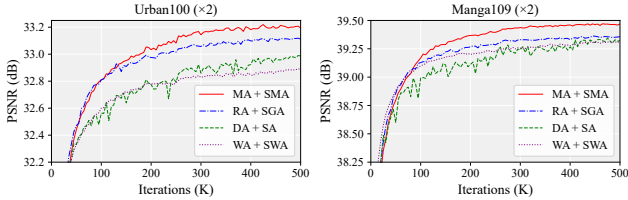


Figure 7: PSNR (dB) comparison of different attention mechanisms on Urban100 and Manga109 datasets.

SwinIR-light with regional attention, while reducing the number of Transformer blocks in each layer to four. We set the range size of regional attention to 9×9 , which is close to the window size of SwinIR-light. We then apply our proposed methods one by one, including capturing multi-range dependencies (MD), introducing MSCConvStar, and implementing multi-range attention (MA). The results clearly show that each proposed component is effective, demonstrating the superiority of capturing multi-range features in the image. Next, we perform individual ablation experiments on each component in reverse order.

Effectiveness of Multi-Range Attention. We conduct a comparative experiment between our MA and other representative attention mechanisms, including window attention (WA) (Liang et al. 2021), sparse attention (SA) (Zhang et al. 2023) and regional attention (RA). As shown in the Fig. 7, the combination of dense attention (DA) and sparse attention (SA) in ART achieves better results compared to the combination of window attention (WA) and shifted window attention (SWA) in SwinIR, demonstrating the effectiveness of sparse operations. Additionally, regional attention (RA) and sparse global attention (SGA) can overcome the shortcomings of window partition in DA and SA, further enhancing model performance. By further expanding RA and SGA into MA and SMA, the model achieves the best performance.

Effectiveness of MSCConvStar. To assess the effectiveness of MSCConvStar, we conduct experiments comparing four different configurations, as depicted in Fig. 4. As shown in Table 5, incorporating depth-wise convolutions into MLP leads to improved performance, highlighting the importance of spatial information. Additionally, the star operation reduces model complexity and enhances its non-linear expression ability, resulting in better performance. Our MSCConvStar further extends a single convolution to multi-scale convolutions to capture multi-range features.

Effectiveness of Multi-range Dependencies. To achieve the integration of multi-range features in MAT, we utilize LAB, MA, and SMA to capture local, regional, and sparse global features, respectively. In order to demonstrate the ef-

Local	Regional	Sparse Global	PSNR (dB) / SSIM
✓	✓	✗	32.94 / 0.9358
✓	✗	✓	33.00 / 0.9366
✗	✓	✓	33.15 / 0.9376
✓	✓	✓	33.22 / 0.9381

Table 6: Ablation study on multi-range dependencies.

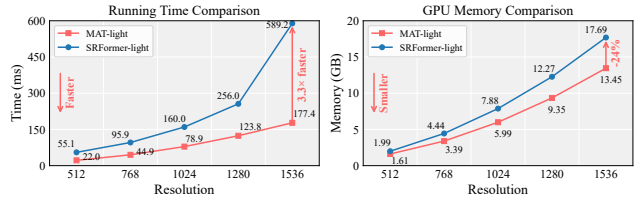


Figure 8: Running time and memory comparisons on $\times 4$ SR.

ficacy of learning multi-range features, we conduct experiments using four different schemes, as outlined in Table 6. It is important to note that we ensure consistency in model parameters by adjusting the number of channels in the 1×1 convolution of MSCConvStar. Our observations reveal that removing any level of feature hierarchy results in a decrease in model performance, with larger range features playing a more significant role.

Running Time and Memory Comparisons

To further illustrate the efficiency of proposed method, we compare MAT-light with the representative Transformer-based model SRFormer-light (Zhou et al. 2023) on SR in terms of running time and GPU memory footprint. The running time is averaged over 100 test images, and the maximum memory consumption of 3090 GPU during the inference process is recorded. As shown in Figs. 8, the SRFormer-light, due to the usage of large windows, involves more padding pixels and shift operations, resulting in longer running time and higher memory consumption. In contrast, our MAT-light achieves significant advantages in both runtime and memory usage. For example, MAT-light is about $3.3\times$ faster than SRFormer-light and saves 24% GPU memory when generating a HR image with a resolution of 1536^2 .

Conclusion

We propose a highly efficient MAT model for image SR tasks. MAT combines the computational properties of dilation operation and self-attention mechanism to achieve multi-range attention mechanism, flexibly adjusting the attention scope and enhancing the perception of regional and sparse global features. Further coupled with local feature extraction, MAT achieves effective multi-range representation learning. Moreover, we propose a simple yet effective MSCConvStar module to augment the image token’s inter-connection. Extensive experiments demonstrate the effectiveness and high efficiency of proposed method. Our MAT achieves SOTA performance in both lightweight and classical SR tasks with lower parameters and computational cost.

References

- Agustsson, E.; and Timofte, R. 2017. Ntire 2017 challenge on single image super-resolution: Dataset and study. In *Proceedings of the IEEE/CVF Conference on Computer Vision and Pattern Recognition (CVPR) Workshops*, 126–135.
- Bevilacqua, M.; Roumy, A.; Guillemot, C.; and Alberi-Morel, M. L. 2012. Low-complexity single-image super-resolution based on nonnegative neighbor embedding. In *Proceedings of the British Machine Vision Conference (BMVC)*.
- Carion, N.; Massa, F.; Synnaeve, G.; Usunier, N.; Kirillov, A.; and Zagoruyko, S. 2020. End-to-end object detection with transformers. In *Proceedings of the European Conference on Computer Vision (ECCV)*, 213–229.
- Chen, L.-C.; Papandreou, G.; Kokkinos, I.; Murphy, K.; and Yuille, A. L. 2017a. Deeplab: Semantic image segmentation with deep convolutional nets, atrous convolution, and fully connected crfs. *IEEE Transactions on Pattern Analysis and Machine Intelligence (TPAMI)*, 40(4): 834–848.
- Chen, L.-C.; Papandreou, G.; Schroff, F.; and Adam, H. 2017b. Rethinking atrous convolution for semantic image segmentation. *arXiv preprint arXiv:1706.05587*.
- Chen, X.; Wang, X.; Zhou, J.; Qiao, Y.; and Dong, C. 2023. Activating more pixels in image super-resolution transformer. In *Proceedings of the IEEE/CVF Conference on Computer Vision and Pattern Recognition (CVPR)*, 22367–22377.
- Choi, H.; Lee, J.; and Yang, J. 2023. N-gram in swin transformers for efficient lightweight image super-resolution. In *Proceedings of the IEEE/CVF Conference on Computer Vision and Pattern Recognition (CVPR)*, 2071–2081.
- Dai, T.; Cai, J.; Zhang, Y.; Xia, S.-T.; and Zhang, L. 2019. Second-order attention network for single image super-resolution. In *Proceedings of the IEEE/CVF Conference on Computer Vision and Pattern Recognition (CVPR)*, 11065–11074.
- Ding, X.; Zhang, X.; Han, J.; and Ding, G. 2022. Scaling up your kernels to 31x31: Revisiting large kernel design in cnns. In *Proceedings of the IEEE/CVF Conference on Computer Vision and Pattern Recognition (CVPR)*, 11963–11975.
- Dong, C.; Loy, C. C.; He, K.; and Tang, X. 2015. Image super-resolution using deep convolutional networks. *IEEE Transactions on Pattern Analysis and Machine Intelligence (TPAMI)*, 38(2): 295–307.
- Dosovitskiy, A.; Beyer, L.; Kolesnikov, A.; Weissenborn, D.; Zhai, X.; Unterthiner, T.; Dehghani, M.; Minderer, M.; Heigold, G.; Gelly, S.; et al. 2021. An image is worth 16x16 words: Transformers for image recognition at scale. In *Proceedings of the International Conference on Learning Representations (ICLR)*.
- Gu, J.; and Dong, C. 2021. Interpreting super-resolution networks with local attribution maps. In *Proceedings of the IEEE/CVF Conference on Computer Vision and Pattern Recognition (CVPR)*, 9199–9208.
- Guo, H.; Li, J.; Dai, T.; Ouyang, Z.; Ren, X.; and Xia, S.-T. 2024. MambaIR: A Simple Baseline for Image Restoration with State-Space Model. In *Proceedings of the European Conference on Computer Vision (ECCV)*.
- Hassani, A.; Walton, S.; Li, J.; Li, S.; and Shi, H. 2023. Neighborhood attention transformer. In *Proceedings of the IEEE/CVF Conference on Computer Vision and Pattern Recognition (CVPR)*, 6185–6194.
- Huang, J.-B.; Singh, A.; and Ahuja, N. 2015. Single image super-resolution from transformed self-exemplars. In *Proceedings of the IEEE/CVF Conference on Computer Vision and Pattern Recognition (CVPR)*, 5197–5206.
- Hui, Z.; Gao, X.; Yang, Y.; and Wang, X. 2019. Lightweight image super-resolution with information multi-distillation network. In *Proceedings of the ACM International Conference on Multimedia (ACM MM)*, 2024–2032.
- Kim, J.; Lee, J. K.; and Lee, K. M. 2016. Accurate image super-resolution using very deep convolutional networks. In *Proceedings of the IEEE/CVF Conference on Computer Vision and Pattern Recognition (CVPR)*, 1646–1654.
- Kingma, D. P.; and Ba, J. 2014. Adam: A method for stochastic optimization. *arXiv preprint arXiv:1412.6980*.
- Li, A.; Zhang, L.; Liu, Y.; and Zhu, C. 2023. Feature modulation transformer: Cross-refinement of global representation via high-frequency prior for image super-resolution. In *Proceedings of the IEEE/CVF International Conference on Computer Vision (ICCV)*, 12514–12524.
- Li, Z.; Liu, Y.; Chen, X.; Cai, H.; Gu, J.; Qiao, Y.; and Dong, C. 2022. Blueprint separable residual network for efficient image super-resolution. In *Proceedings of the IEEE/CVF Conference on Computer Vision and Pattern Recognition (CVPR) Workshops*, 833–843.
- Liang, J.; Cao, J.; Sun, G.; Zhang, K.; Van Gool, L.; and Timofte, R. 2021. Swinir: Image restoration using swin transformer. In *Proceedings of the IEEE/CVF International Conference on Computer Vision (ICCV) Workshops*, 1833–1844.
- Lim, B.; Son, S.; Kim, H.; Nah, S.; and Mu Lee, K. 2017. Enhanced deep residual networks for single image super-resolution. In *Proceedings of the IEEE/CVF Conference on Computer Vision and Pattern Recognition (CVPR) Workshops*, 136–144.
- Liu, Z.; Lin, Y.; Cao, Y.; Hu, H.; Wei, Y.; Zhang, Z.; Lin, S.; and Guo, B. 2021. Swin transformer: Hierarchical vision transformer using shifted windows. In *Proceedings of the IEEE/CVF International Conference on Computer Vision (ICCV)*, 10012–10022.
- Luo, X.; Xie, Y.; Zhang, Y.; Qu, Y.; Li, C.; and Fu, Y. 2020. Latticenet: Towards lightweight image super-resolution with lattice block. In *Proceedings of the European Conference on Computer Vision (ECCV)*, 272–289.
- Ma, X.; Dai, X.; Bai, Y.; Wang, Y.; and Fu, Y. 2024. Rewrite the Stars. In *Proceedings of the IEEE/CVF Conference on Computer Vision and Pattern Recognition (CVPR)*, 5694–5703.

- Martin, D.; Fowlkes, C.; Tal, D.; and Malik, J. 2001. A database of human segmented natural images and its application to evaluating segmentation algorithms and measuring ecological statistics. In *Proceedings of the IEEE/CVF International Conference on Computer Vision (ICCV)*, volume 2, 416–423.
- Matsui, Y.; Ito, K.; Aramaki, Y.; Fujimoto, A.; Ogawa, T.; Yamasaki, T.; and Aizawa, K. 2017. Sketch-based manga retrieval using manga109 dataset. *Multimedia Tools and Applications*, 76: 21811–21838.
- Mei, Y.; Fan, Y.; and Zhou, Y. 2021. Image super-resolution with non-local sparse attention. In *Proceedings of the IEEE/CVF Conference on Computer Vision and Pattern Recognition (CVPR)*, 3517–3526.
- Ramachandran, P.; Parmar, N.; Vaswani, A.; Bello, I.; Levskaya, A.; and Shlens, J. 2019. Stand-alone self-attention in vision models. *Advances in Neural Information Processing Systems (NeurIPS)*, 32.
- Redmon, J.; and Farhadi, A. 2018. Yolov3: An incremental improvement. *arXiv preprint arXiv:1804.02767*.
- Shi, W.; Caballero, J.; Huszár, F.; Totz, J.; Aitken, A. P.; Bishop, R.; Rueckert, D.; and Wang, Z. 2016. Real-time single image and video super-resolution using an efficient sub-pixel convolutional neural network. In *Proceedings of the IEEE/CVF Conference on Computer Vision and Pattern Recognition (CVPR)*, 1874–1883.
- Vaswani, A.; Ramachandran, P.; Srinivas, A.; Parmar, N.; Hechtman, B.; and Shlens, J. 2021. Scaling local self-attention for parameter efficient visual backbones. In *Proceedings of the IEEE/CVF Conference on Computer Vision and Pattern Recognition (CVPR)*, 12894–12904.
- Vaswani, A.; Shazeer, N.; Parmar, N.; Uszkoreit, J.; Jones, L.; Gomez, A. N.; Kaiser, Ł.; and Polosukhin, I. 2017. Attention is all you need. *Advances in Neural Information Processing Systems (NeurIPS)*, 30.
- Wang, H.; Chen, X.; Ni, B.; Liu, Y.; and Liu, J. 2023. Omni Aggregation Networks for Lightweight Image Super-Resolution. In *Proceedings of the IEEE/CVF Conference on Computer Vision and Pattern Recognition (CVPR)*, 22378–22387.
- Wang, P.; Chen, P.; Yuan, Y.; Liu, D.; Huang, Z.; Hou, X.; and Cottrell, G. 2018a. Understanding convolution for semantic segmentation. In *Proceedings of the IEEE/CVF Winter Conference on Applications of Computer Vision (WACV)*, 1451–1460.
- Wang, X.; Girshick, R.; Gupta, A.; and He, K. 2018b. Non-local neural networks. In *Proceedings of the IEEE/CVF Conference on Computer Vision and Pattern Recognition (CVPR)*, 7794–7803.
- Xia, B.; Hang, Y.; Tian, Y.; Yang, W.; Liao, Q.; and Zhou, J. 2022. Efficient non-local contrastive attention for image super-resolution. In *Proceedings of the AAAI Conference on Artificial Intelligence (AAAI)*, volume 36, 2759–2767.
- Xie, C.; Zhang, X.; Li, L.; Meng, H.; Zhang, T.; Li, T.; and Zhao, X. 2023. Large Kernel Distillation Network for Efficient Single Image Super-Resolution. In *Proceedings of the IEEE/CVF Conference on Computer Vision and Pattern Recognition (CVPR) Workshops*, 1283–1292.
- Xie, E.; Wang, W.; Yu, Z.; Anandkumar, A.; Alvarez, J. M.; and Luo, P. 2021. SegFormer: Simple and efficient design for semantic segmentation with transformers. *Advances in Neural Information Processing Systems (NeurIPS)*, 34: 12077–12090.
- Zamir, S. W.; Arora, A.; Khan, S.; Hayat, M.; Khan, F. S.; and Yang, M.-H. 2022. Restormer: Efficient transformer for high-resolution image restoration. In *Proceedings of the IEEE/CVF Conference on Computer Vision and Pattern Recognition (CVPR)*, 5728–5739.
- Zeyde, R.; Elad, M.; and Protter, M. 2012. On single image scale-up using sparse-representations. In *Proceedings of the International Conference of Curves and Surfaces*, 711–730.
- Zhang, J.; Zhang, Y.; Gu, J.; Zhang, Y.; Kong, L.; and Yuan, X. 2023. Accurate Image Restoration with Attention Retractable Transformer. In *Proceedings of the International Conference on Learning Representations (ICLR)*.
- Zhang, X.; Li, T.; and Zhao, X. 2023. Boosting Single Image Super-Resolution via Partial Channel Shifting. In *Proceedings of the IEEE/CVF International Conference on Computer Vision (ICCV)*, 13223–13232.
- Zhang, Y.; Li, K.; Li, K.; Wang, L.; Zhong, B.; and Fu, Y. 2018a. Image super-resolution using very deep residual channel attention networks. In *Proceedings of the European Conference on Computer Vision (ECCV)*, 286–301.
- Zhang, Y.; Tian, Y.; Kong, Y.; Zhong, B.; and Fu, Y. 2018b. Residual dense network for image super-resolution. In *Proceedings of the IEEE/CVF Conference on Computer Vision and Pattern Recognition (CVPR)*, 2472–2481.
- Zhou, S.; Zhang, J.; Zuo, W.; and Loy, C. C. 2020. Cross-scale internal graph neural network for image super-resolution. *Advances in Neural Information Processing Systems (NeurIPS)*, 33: 3499–3509.
- Zhou, Y.; Li, Z.; Guo, C.-L.; Bai, S.; Cheng, M.-M.; and Hou, Q. 2023. SRFormer: Permuted Self-Attention for Single Image Super-Resolution. In *Proceedings of the IEEE/CVF International Conference on Computer Vision (ICCV)*, 12780–12791.

MAT: Multi-Range Attention Transformer for Efficient Image Super-Resolution

Supplementary Material

In this supplementary, we provide the following three parts: (1) We provide the ERF visualization of lightweight image SR models. (2) We conduct the LAM analysis of lightweight image SR models. (3) We provide more comparison results between MAT and classical image SR models.

ERF Visualization

To demonstrate the effectiveness of multi-range attention, we use the Effective Receptive Field (ERF) (Ding et al. 2022) to measure the actual receptive field of the model. We compare the ERF visualization of our MAT-light with other advanced lightweight methods on $\times 4$ SR. When different thresholds are set for the total weight of ERF, the comparison of the Area Ratio (AR) and Rectangular Side Length (RSL) of ERF is shown in Fig. 9. It can be observed that the CNN-based model EDSR-baseline has the smallest ERF, highlighting the limitations of CNNs in capturing long-range dependencies. Even when compared to SRFormer-light, which uses a large window of 16×16 , our MAT-light exhibits the largest ERF, allowing it to perceive a wider range of information.

LAM Analysis

In order to further demonstrate the effectiveness of our MAT, we use Local Attribution Map (LAM) (Gu and Dong 2021) to analyze the model’s ability to use information. As shown in Fig. 10, we compare the LAM results of our MAT-light with other advanced lightweight methods on $\times 4$ SR. The LAM attribution of MAT-light extends across nearly the entire image, whereas other models are confined to a limited range. In terms of quantitative metrics, MAT-light also achieves a significantly higher Diffusion Index (DI) value compared to other models. These result indicate that MAT is capable of utilizing more information for reconstruction, resulting in optimal performance, and demonstrates its effectiveness in capturing features across various spatial scales.

Classical Image Super-Resolution

To demonstrate our model’s scalability, we further scale up MAT to build a large model and compare it with a series of state-of-the-art classical SR methods: EDSR (Lim et al. 2017), RDN (Zhang et al. 2018b), RCAN (Zhang et al. 2018a), IGNN (Zhou et al. 2020), NLSN (Mei, Fan, and Zhou 2021), SwinIR (Liang et al. 2021), ART (Zhang et al. 2023), SRFormer (Zhou et al. 2023) and MambaIR (Guo et al. 2024). Consistent with prior works (Liang et al. 2021; Zhou et al. 2023; Guo et al. 2024), self-ensemble strategy is introduced in testing to further improve the model’s performance, denoted by the symbol “+”.

Implementation Details. For the classical image SR, the number of the RMAG, MAB and channel increase to 6, 3,

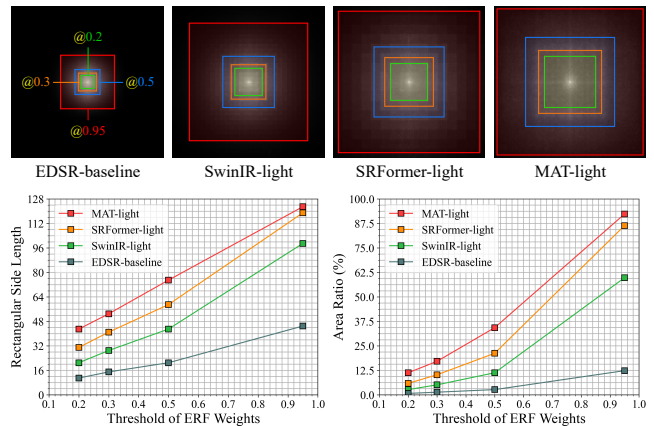


Figure 9: The ERF (Ding et al. 2022) visualization and comparison for EDSR-baseline (Lim et al. 2017), SwinIR-light (Liang et al. 2021), SRFormer-light (Zhou et al. 2023), and the proposed MAT-light. A larger ERF is indicated by a more extensively distributed bright area.

and 156, respectively. The range sizes of MA and SMA increase to 13×13 , 15×15 and 17×17 , respectively. The number of attention heads is set to 6. For data augmentation, we randomly rotate and horizontally flip the input patches. We employ Adam (Kingma and Ba 2014) optimizer with $\beta_1 = 0.9$ and $\beta_2 = 0.99$ to train the model for a total of 500k iterations. The initial learning rate is set at 2×10^{-4} and is halved at [250k, 400k, 450k, 475k].

Quantitative Comparison. Table 7 displays the quantitative comparison for classical image SR models. It can be observed that MAT achieves optimal performance for all scale factors with the minimal parameter count and computational complexity on all five benchmark datasets. By utilizing a multi-range attention mechanism and multi-range feature modeling, MAT can flexibly perceive various hierarchical features of images. The performance improvement of MAT is more significant when self-ensemble strategy is used. The above results strongly demonstrate the effectiveness and scalability of MAT.

Visual Comparison. We also provide the visual comparison of our MAT with other classical image SR models, as shown in Fig. 11. It can be observed that only the images restored by our MAT have clear lines and consistent textures. With the ability to perceive features across various spatial ranges, MAT possesses powerful detail reconstruction capabilities.

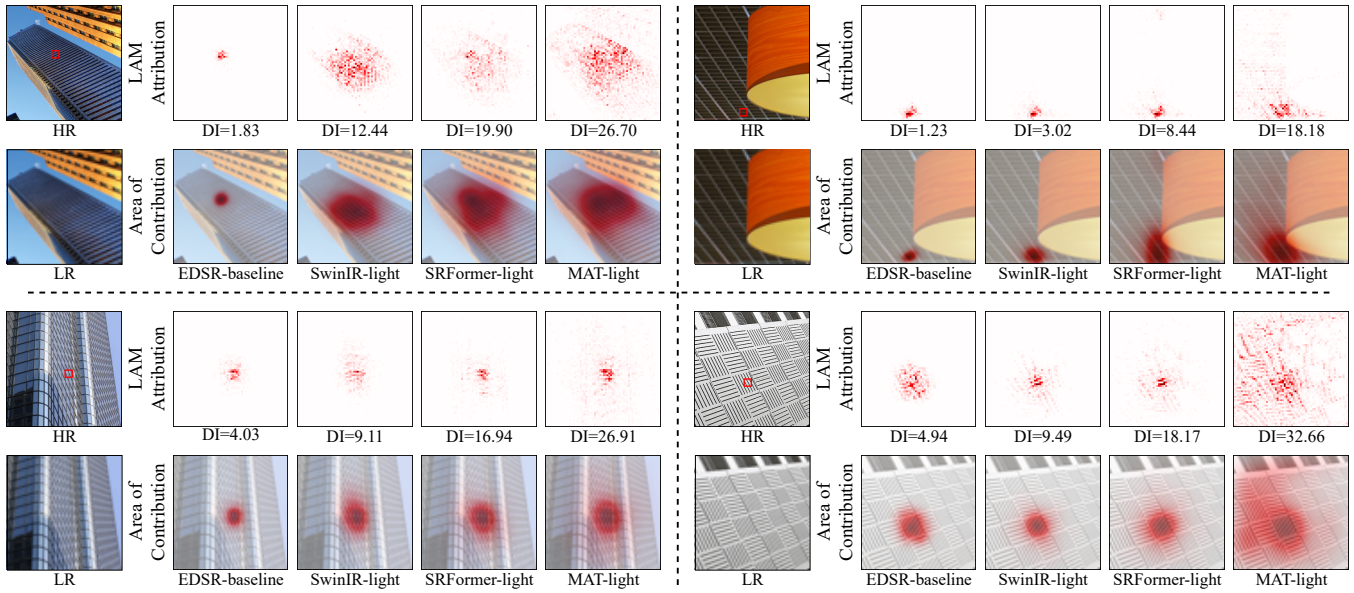


Figure 10: The LAM results of EDSR-baseline (Lim et al. 2017), SwinIR-light (Liang et al. 2021), SRFormer-light (Zhou et al. 2023), and the proposed MAT-light. A higher diffusion index (DI) indicates a broader range of pixels available to the model.

Scale	Method	Annual	Params. (M)	Multi-Adds (G)	Set5 PSNR / SSIM	Set14 PSNR / SSIM	B100 PSNR / SSIM	Urban100 PSNR / SSIM	Manga109 PSNR / SSIM
×2	EDSR	CVPRW17	40.73	667.4	38.11 / 0.9602	33.92 / 0.9195	32.32 / 0.9013	32.93 / 0.9351	39.10 / 0.9773
	RCAN	ECCV18	15.44	251.0	38.27 / 0.9614	34.12 / 0.9216	32.41 / 0.9027	33.34 / 0.9384	39.44 / 0.9786
	IGNN	NeurIPS20	49.51	-	38.24 / 0.9613	34.07 / 0.9217	32.41 / 0.9025	33.23 / 0.9383	39.35 / 0.9786
	NLSN	CVPR21	41.80	731.4	38.34 / 0.9618	34.08 / 0.9231	32.43 / 0.9027	33.42 / 0.9394	39.59 / 0.9789
	SwinIR	ICCV21	11.75	205.3	38.42 / 0.9623	34.46 / 0.9250	32.53 / 0.9041	33.81 / 0.9427	39.92 / 0.9797
	ART-S	ICLR23	11.71	227.6	38.48 / 0.9625	34.50 / 0.9258	32.53 / 0.9043	34.02 / 0.9437	40.11 / 0.9804
	SRFormer	ICCV23	10.38	206.4	38.51 / 0.9627	34.44 / 0.9253	32.57 / 0.9046	34.09 / 0.9449	40.07 / 0.9802
	MambaIR	ECCV24	20.42	318.8	38.57 / 0.9627	<u>34.67 / 0.9261</u>	32.58 / 0.9048	34.15 / 0.9446	<u>40.28 / 0.9806</u>
	MAT	Ours	9.60	187.0	<u>38.61 / 0.9631</u>	34.53 / 0.9259	<u>32.62 / 0.9053</u>	<u>34.31 / 0.9462</u>	<u>40.22 / 0.9808</u>
	MAT+	Ours	9.60	187.0	38.65 / 0.9632	34.60 / 0.9263	32.65 / 0.9056	34.44 / 0.9468	40.33 / 0.9811
×3	EDSR	CVPRW17	43.68	315.9	34.65 / 0.9280	30.52 / 0.8462	29.25 / 0.8093	28.80 / 0.8653	34.17 / 0.9476
	RCAN	ECCV18	15.63	112.1	34.74 / 0.9299	30.65 / 0.8482	29.32 / 0.8111	29.09 / 0.8702	34.44 / 0.9499
	IGNN	NeurIPS20	49.51	-	34.72 / 0.9298	30.66 / 0.8484	29.31 / 0.8105	29.03 / 0.8696	34.39 / 0.9496
	NLSN	CVPR21	44.75	344.1	34.85 / 0.9306	30.70 / 0.8485	29.34 / 0.8117	29.25 / 0.8726	34.57 / 0.9508
	SwinIR	ICCV21	11.94	98.5	34.97 / 0.9318	30.93 / 0.8534	29.46 / 0.8145	29.75 / 0.8826	35.12 / 0.9537
	ART-S	ICLR23	11.90	102.0	34.98 / 0.9318	30.94 / 0.8530	29.45 / 0.8146	29.86 / 0.8830	35.22 / 0.9539
	SRFormer	ICCV23	10.56	93.2	35.02 / 0.9323	30.94 / 0.8540	29.48 / 0.8156	30.04 / 0.8865	35.26 / 0.9543
	MambaIR	ECCV24	20.61	142.0	35.08 / 0.9323	30.99 / 0.8536	29.51 / 0.8157	29.93 / 0.8841	<u>35.43 / 0.9546</u>
	MAT	Ours	9.78	83.9	<u>35.09 / 0.9328</u>	31.03 / 0.8550	<u>29.53 / 0.8167</u>	30.11 / 0.8879	35.41 / 0.9549
	MAT+	Ours	9.78	83.9	35.13 / 0.9330	31.08 / 0.8555	29.56 / 0.8171	30.22 / 0.8893	35.55 / 0.9554
×4	EDSR	CVPRW17	43.09	205.8	32.46 / 0.8968	28.80 / 0.7876	27.71 / 0.7420	26.64 / 0.8033	31.02 / 0.9148
	RCAN	ECCV18	15.59	65.3	32.63 / 0.9002	28.87 / 0.7889	27.77 / 0.7436	26.82 / 0.8087	31.22 / 0.9173
	IGNN	NeurIPS20	49.51	-	32.57 / 0.8998	28.85 / 0.7891	27.77 / 0.7434	26.84 / 0.8090	31.28 / 0.9182
	NLSN	CVPR21	44.16	221.8	32.59 / 0.9000	28.87 / 0.7891	27.78 / 0.7444	26.96 / 0.8109	31.27 / 0.9184
	SwinIR	ICCV21	11.90	53.8	32.92 / 0.9044	29.09 / 0.7950	27.92 / 0.7489	27.45 / 0.8254	32.03 / 0.9260
	ART-S	ICLR23	11.87	55.6	32.86 / 0.9029	29.09 / 0.7942	27.91 / 0.7489	27.54 / 0.8261	32.13 / 0.9263
	SRFormer	ICCV23	10.52	54.3	32.93 / 0.9041	29.08 / 0.7953	27.94 / 0.7502	27.68 / 0.8311	32.21 / 0.9271
	MambaIR	ECCV24	20.57	82.2	33.03 / 0.9046	<u>29.20 / 0.7961</u>	27.98 / 0.7503	27.68 / 0.8287	<u>33.32 / 0.9272</u>
	MAT	Ours	9.74	49.2	<u>33.06 / 0.9054</u>	29.17 / 0.7960	<u>27.99 / 0.7514</u>	<u>27.78 / 0.8328</u>	<u>32.31 / 0.9282</u>
	MAT+	Ours	9.74	49.2	33.08 / 0.9056	29.24 / 0.7972	28.02 / 0.7520	27.89 / 0.8349	32.49 / 0.9294

Table 7: Quantitative comparison (PSNR (dB) / SSIM) with state-of-the-art methods for **classical SR** on five benchmark datasets. 'Multi-Adds' is calculated under the setting of upscaling one image to 256^2 resolution. The best and second best results are marked in bold and underline, respectively.

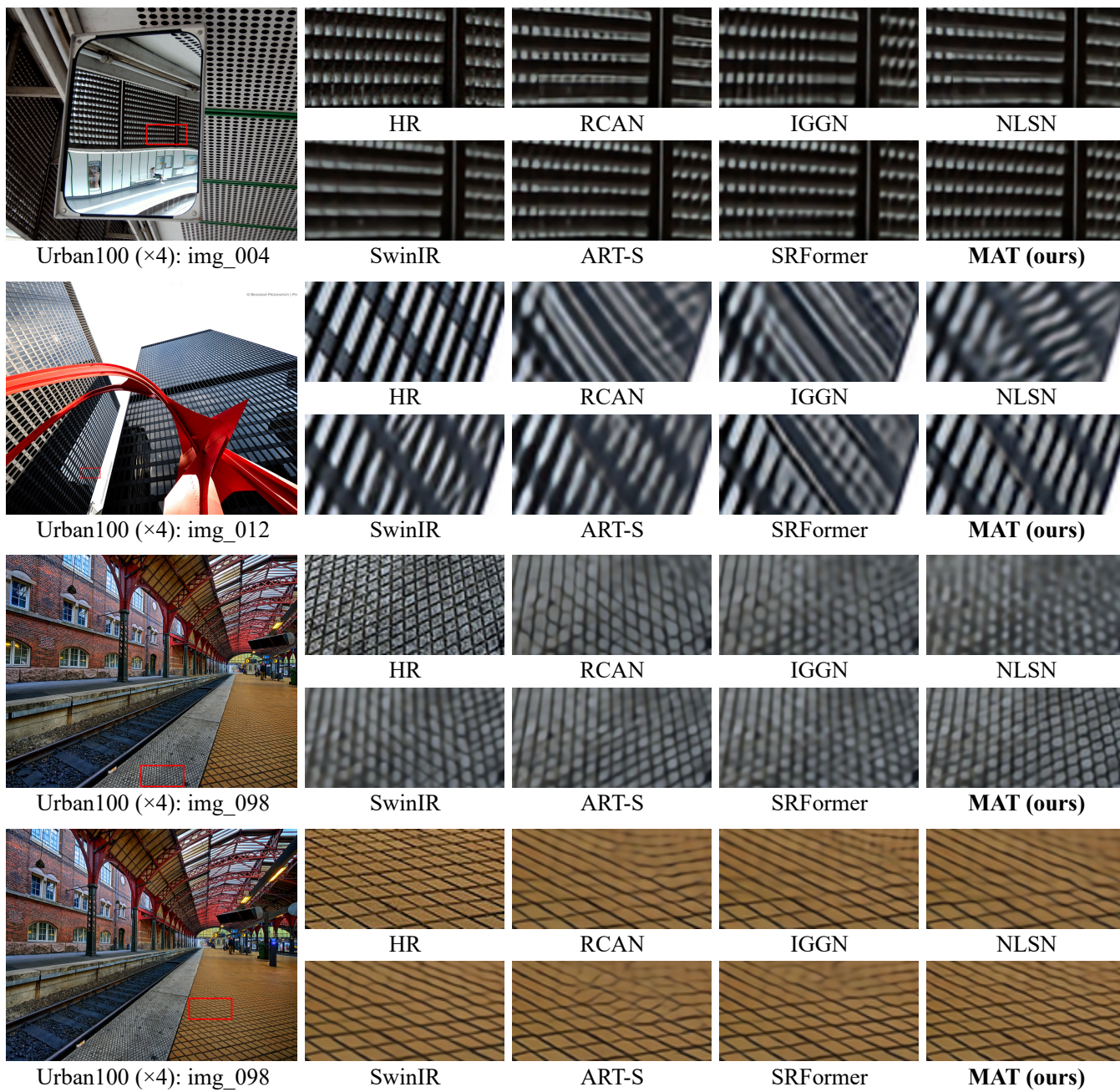


Figure 11: Visual comparison on $\times 4$ classical image SR.